Rijksuniversiteit Groningen

Faculteit der Wiskunde en Natuurwetenschappen

Heat transport measurements in spin-ladder compounds

BACHELOR THESIS BY: Morten Bakker

Research Group: Optical Condensed Matter Physics

Supervisor: M. Otter, Prof. dr. ir. P.H.M. van Loosdrecht

Period: May 2008 – August 2008

Contents

1 Introduction

In 1994 it was firstly confirmed by Eccleston *et. al.* [1] that some solids contain a spatial structure called a Heisenberg antiferromagnetic spin ladder, in which spins of electrons are ordered in a specific way.

Disturbances in the spin ordering can propagate as waves in the medium, so-called spin waves. The energy of spin waves is quantized and a quantum of a magnetic excitation is a quasi particle, called a magnon. Magnons were firstly described by Felix Bloch in 1930 [2].

The spin ladder materials were initially of high interest because of their superconductive properties at high temperatures [3]. Recently, in 2001, it was found that such materials conduct heat in an anisotropic manner [4]. This special property opens new possibilities for thermal management, especially in microelectronics. Novel magnetic-mode heat transport for thermal management in microelectronics (NOVMAG) is a consortium of several European research teams funded by the European Union, which aims at research, development and application of such materials [5]. The present work was performed in the Optical Condensed Matter Physics group, led by Prof. dr. ir. Paul H. M. van Loosdrecht. The main goal of the current project is the optical investigation of heat conduction in spin ladder compounds.

In the present work the measurements were performed on a $Ca_9La_5Cu_{24}O_{41}$ and a $La_4Sr_{10}Cu_{24}O_{41}$ sample. Also measurements on nickel were performed since the heat conductive properties of this material are well documented [6]. The experiment presented in the current report is based on the fluorescent microthermal imaging technique. This technique has a high potential to perform measurements on bulk materials and thin films and study their heat conductive properties.

Using equations for heat diffusion in three dimensions a simulation is developed. Based on the results of the experiment and consequent simulations the values for the diffusion constants are derived. The results clearly show the anisotropic manner of heat transport for the spin ladder compounds. However the values do not correspond with ones, previously reported [4, 6, 27, 23], and possible origins will be discussed.

2 Theoretical background

2.1 Heat transport in spin ladder compounds

The crystals $Ca_9La_5Cu_{24}O_{41}$ and $La_4Sr_{10}Cu_{24}O_{41}$ on which measurements were performed, belong to a group of materials, denoted $(Sr, La, Ca)_{14}Cu_{24}O_{41}$, known as low dimensional quantum magnets. The name refers to the presence of nearly one dimensional anti-ferromagnetic spin ladders, along which quantized spin waves can transport heat.

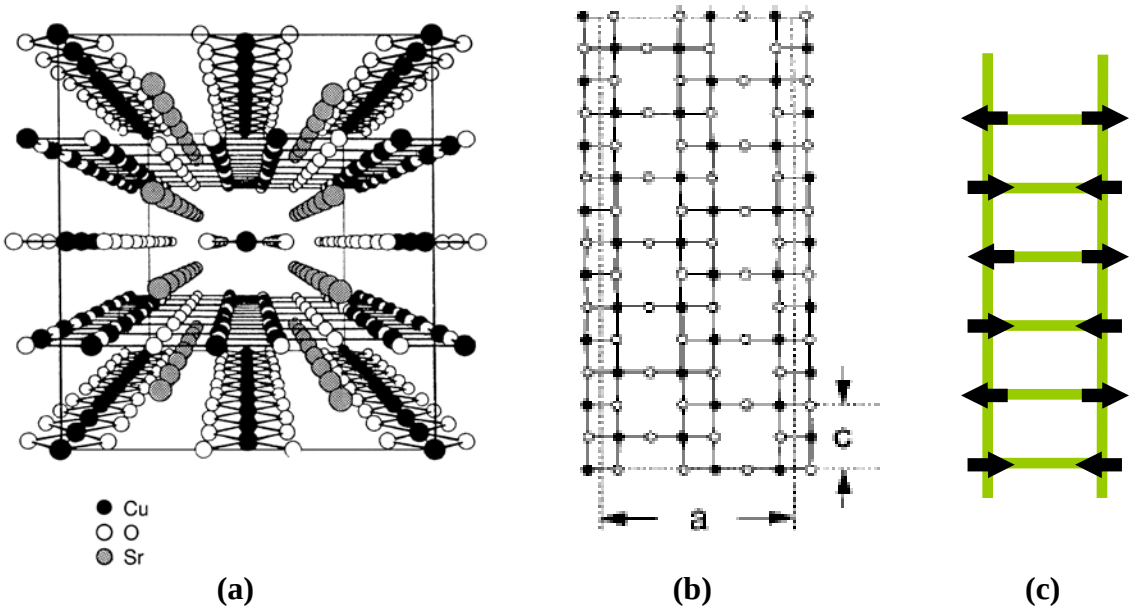

Fig 2.1. (a) Schematic picture of the crystal structure of $(Sr, La, Ca)_{14}Cu_{24}O_{41}$. It contains in the c-direction (perpendicular to the plane) 2-d sheets in which spin ladders are lying side by side. (b) Over the distance <-a-> there are two ladders. c is the distance between the rungs. (c) Schematic representation how the spins of the Cu-ions in a spin ladder are aligned anti-ferromagnetically below T_N. Figures (a) and (b) are reproduced from [22].

The crystal structure of the investigated spin ladder compounds is presented in Fig 2.1 (a,b). The spin ladders consist of Cu^{2+}-ions connected by O^{2-}-ions. The Cu-ions (normal electron configuration $3d^{10}4s$) are doubly ionized so they have the electron configuration $3d^9$, which has spin S=½. Due to the properties of the crystal, it is energetically favorable for these spins to be anti-ferromagnetically aligned below a certain ordering temperature or Néel temperature T_N (Fig 2 c). At temperatures higher than T_N there is still some correlation between spins in the chain.

An excitation in this spin ladder, a magnon with spin S=1, requires an energy of about $\Delta \approx 0.034$ eV [9]. These magnons travel along the spin ladders, thereby transporting energy and thus conduct heat.

There are two properties that make such materials interesting:

- Weak interaction between the spin ladders, 180° Cu-O-Cu interaction (for Cu-ions in a spin ladder) >> 90° Cu-O-Cu interaction (Cu-ions between different

ladders) [30], causes the magnons to transport energy only along the spin ladder direction (c-axis).

- Since the magnon interactions require conservation of energy, momentum and spin, the mean free path of the magnons has to be sufficiently long, it was measured to be up to 3000 Å [8]. This property makes magnons very effective heat carriers compared to phonons.

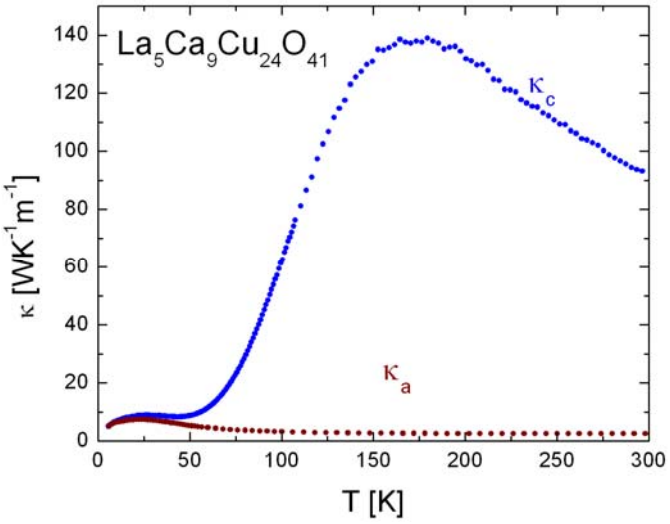

Fig 2.2. Temperature dependence of the thermal conductivity κ of $La_5Ca_9Cu_{24}O_{41}$. κ_c is the thermal conductivity along the spin ladders (c-direction, see Fig 1 a,b) and κ_a is the thermal conductivity perpendicular to the spin ladder direction (a-direction). The figure is reproduced from [4].

For T<40 K, the thermal conductivity along (κ_c) and perpendicular (κ_a) to the direction of the spin ladder are originated from the phonon heat transport, having a maximum at 25 K (Fig 2.2). Since the phonon scattering increases with the raising of the temperature, thereby reducing the mean free path of the particles, the value of κ_a decreases with the temperature. However, along the c-direction, the magnon transport mainly contributes to the heat conduction for T>50 K.

For low T the mean free path of magnons is only dependent on scattering by static defects in the spin ladder chains. The number of magnons increases due to thermal excitations, so for low T, $\kappa_c \sim \exp(-\Delta/kT)$. For higher T the mean free path decreases, hereby reducing κ_c. There are several scattering mechanisms which might play a role:

- Scattering on defects in the spin ladders. The amount of defects can be reduced by careful growing of the crystal.
- Scattering on holes in the spin ladders in high T_c superconductors. By varying the relation of $(Sr, La, Ca)_{14}$ these holes are removed, thereby reducing the electrical conductance and improving heat conductance. The ladders in $La_5Ca_9Cu_{24}O_{41}$ for example are hole free.
- Magnon-magnon and magnon-phonon scattering mechanisms. Experiments seem to suggest magnon-phonon scattering is more dominant, but these scattering mechanisms are still not fully understood and subject of further investigation [9].

The highest value for the thermal conductivity along the c-direction for $La_5Ca_9Cu_{24}O_{41}$ has been found $\kappa_c \sim 100\ WK^{-1}m^{-1}$ around the room temperature [4]. Like the $La_5Ca_9Cu_{24}O_{41}$ compound, $La_4Sr_{10}Cu_{24}O_{41}$ also contains hole free spin ladders. Magnons are expected to have a long mean free path, making this system of interest for heat transport investigation.

2.2 Heat Diffusion

Heat conduction in a material can be described using Fourier's Law, which states that the time rate of heat transfer is proportional to the negative gradient of the temperature, so:

$$\vec{J} = -\kappa\vec{\nabla}T\,, \tag{2.1}$$

where $\vec{J}$ is the heat flux and κ is the thermal conductivity. The change in energy is equal to the sum of the in- and outgoing flux plus the amount of heat P(t) externally added or removed. Because the change in energy δU/δt is also equal to the change in temperature times the density and specific heat at constant pressure, it follows that:

$$\begin{aligned}\frac{\partial U}{\partial t} = \rho C_p \frac{\partial T}{\partial t} = -\vec{\nabla}\vec{J} + P(t) = \vec{\nabla}\left(\kappa\vec{\nabla}T\right) + P(t) = \\ \frac{\partial}{\partial x}\left(\kappa_x \frac{\partial T}{\partial x}\right) + \frac{\partial}{\partial y}\left(\kappa_y \frac{\partial T}{\partial y}\right) + \frac{\partial}{\partial z}\left(\kappa_z \frac{\partial T}{\partial z}\right) + P(t)\end{aligned}\,, \tag{2.2}$$

where ρ is the density and C_p is the specific heat capacity at constant pressure. From Equation (1.2) it follows that:

$$\frac{\partial T}{\partial t} = \sum_{x,y,z}\frac{\partial}{\partial i}\left(D_i(T)\frac{\partial T}{\partial i}\right) + \frac{P(t)}{\rho C_p} = \sum_{x,y,z} D_i(T)\frac{\partial^2 T}{\partial i^2} + \frac{\partial D_i(T)}{\partial T}\left(\frac{\partial T}{\partial i}\right) + \frac{P(t)}{\rho C_p} \tag{2.3}$$

where $D(T) = \dfrac{\kappa(T)}{\rho(T)C_p(T)}$ is the diffusion constant.

If the sample is only heated several Kelvin the diffusion constant can be assumed to remain the same value. The final differential equation for the change in temperature becomes:

$$\frac{\partial T}{\partial t} = \sum_{x,y,z} D_i \frac{\partial^2 T}{\partial i^2} + \frac{P(t)}{\rho C_p} \tag{2.4}$$

In cylindrical coordinates ($D_r = D_x = D_y$), the equation (2.4) can be rewritten as:

$$\frac{\partial \mathrm{T}}{\partial \mathrm{t}} = D_r \frac{\partial^2 T}{\partial r^2} + D_r \frac{1}{r}\frac{\partial T}{\partial r} + D_z \frac{\partial^2 T}{\partial z^2} + \frac{P(t)}{\rho C_p} \tag{2.5}$$

In the case of the fcc cubic nickel lattice, the diffusion constant is isotropic, meaning the value of the diffusion constant is the same in all directions.

In the case of more complicated spin ladder compounds, the thermal conductivity is assumed to be the same in the x- and y-direction (a- and b-direction, from Fig 2.1 a,b), however different in the z-direction (c-direction, along the spin ladder). Thus in such materials the heat conductivity has an anisotropic behavior.

3 Experimental Idea and Technique

3.1 Outline of the experiment

Briefly, the main goal of the experiment was to measure how fast heat is transported through a bulk material. For this purpose one can heat the bulk sample by intensive laser light and monitor the temperature change on the other side in real time. This method is similar to the flash method, firstly described in 1961 [28].

To measure such temperature change a special technique is required. During a similar experiment in 2002 the optical reflectivity technique was used [29]. Instead we used fluorescent microthermal imaging (FMI) [10,11]. This technique is based on the temperature dependence of the photoluminescence intensity for certain materials. One of the main popular materials to be used is the rare earth chelate europium thenoyltrifluoroaceteonate (EuTTA). It can be excited in the ultra-violet energy region with a consequent emission in the visible range. The photoluminescence intensity for EuTTA is strongly temperature dependent as announced in literature [12] and will be shown below.

The idea of the experiment is shown in Fig 3.1. The sample was heated by an intense laser beam from one side. On the opposite side, a thin EuTTA layer was coated. The ultra-violet radiation induces luminescence of EuTTA on this side. Since the intensity of the photoluminescence is temperature dependent one can monitor its intensity, i.e. the temperature, as a function of time.

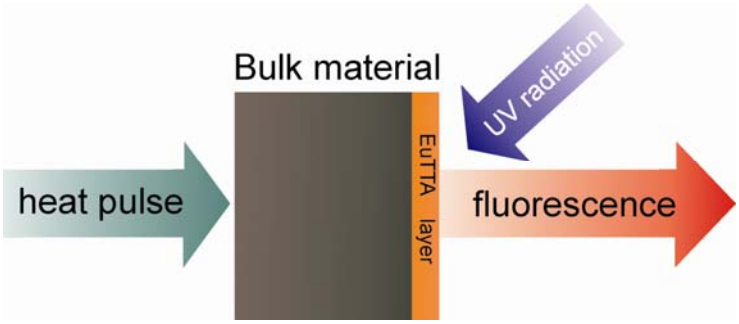

Fig 3.1. Experimental idea.

3.2 Sample handling and preparation

The $Ca_9La_5Cu_{24}O_{41}$ and $La_4Sr_{10}Cu_{24}O_{41}$ crystals used in the experiments are grown using the floating-zone technique [13,14] and were provided by the group of A.Revcolevschi, University of Paris IV. The $Ca_9La_5Cu_{24}O_{41}$, $La_4Sr_{10}Cu_{24}O_{41}$ crystals and the nickel sample were polished to a surface roughness approximately of 1 μm . For better coating, to let the EuTTA remain in place on a surface, it is mixed with deuterated-polymethylmethacrylate (dPMMA), so it will be incorporated in a matrix, but in principle other polymers can also be used.

A mixture of chlorobenzene with EuTTA and dPMMA dissolved was prepared in the relative mass proportion 96.7%:1.41%:1.90%. According to [10,11] a proportion of EuTTA:PMMA equal to 1:1.5 would be optimal. The mixture was prepared in a proportion of 1:1.36. This mixture was coated using a spin coating technique on the $Ca_9La_5Cu_{24}O_{41}$, $La_4Sr_{10}Cu_{24}O_{41}$ and nickel samples and on a glass plate during 2 minutes at 600 rpm. Afterwards the samples were treated in a oven for 30 min. at 125°C, so the chlorobenzene would completely evaporate. This was done in the group Organic Semiconductors, University of Groningen.

The glass plate was used as a reference to determine the layer thickness of the EuTTA-dPMMA matrix layer. Using a "low-force sensing probe"-microscope, the layer thickness was found to be approximately 50 nm. It cannot be assumed the thickness on the other samples is the same, as the thickness is largely determined by the binding of the mixture to the underground, but this measurement can give the order of magnitude of the layer thickness.

3.3 Optical properties of EuTTA

The emission spectrum for EuTTA in crystalline form is presented in Fig 3.2. [15]. We performed an experiment to measure the emission spectrum on layers of EuTTA, incorporated by dPMMA, on the nickel sample and on the $La_4Sr_{10}Cu_{24}O_{41}$ crystal. The experiment was carried out using a luminescence spectrometer (Perkin Elmer LS 50 B).

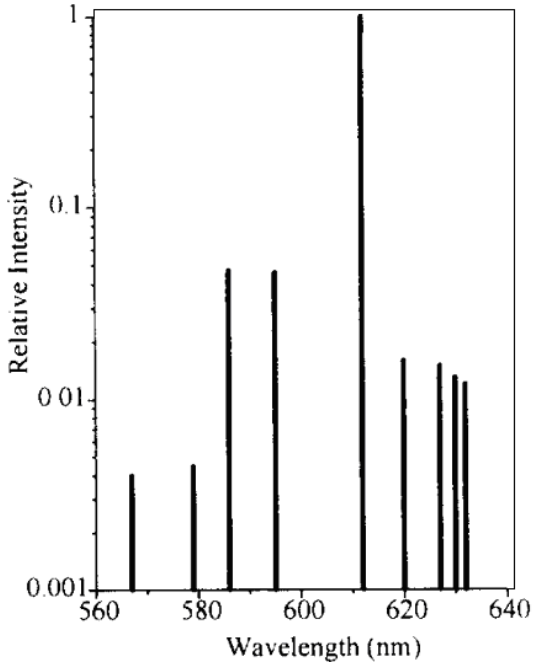

Fig 3.2. Emmision spectrum of EuTTA (crystalline) at 25°C. It was presented in [15].

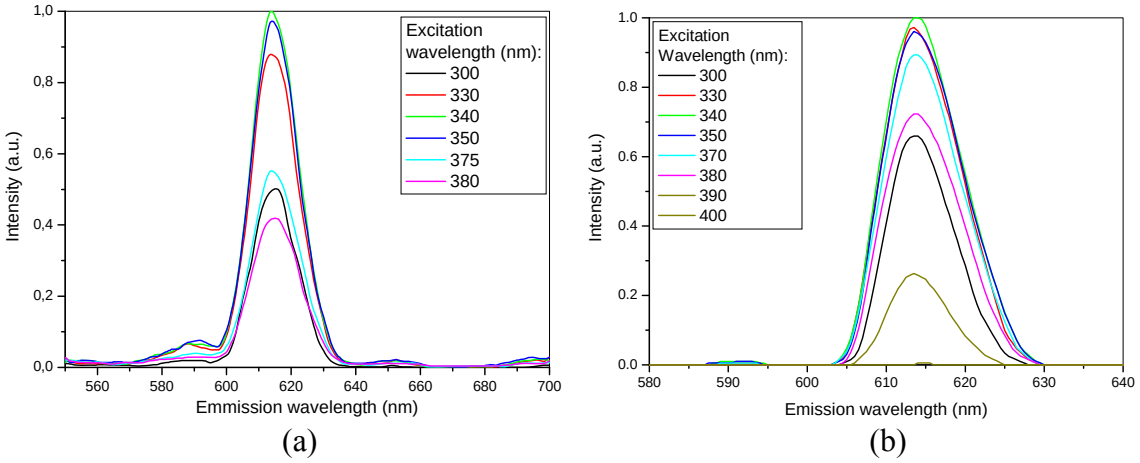

Fig 3.3. (a) - Emission spectrum of the EuTTA-dPMMA layer on the nickel sample.
(b) - Emission spectrum of the EuTTA-dPMMA layer on the $La_4Sr_{10}Cu_{24}O_{41}$ crystal.

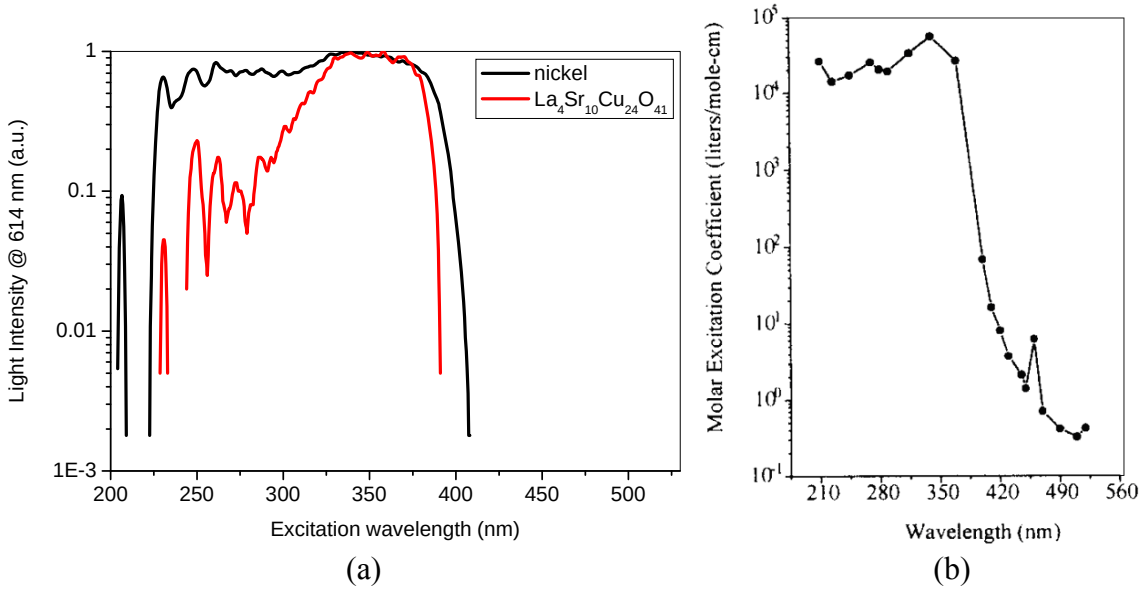

Fig 3.4. (a) – Excitation spectrum of the EuTTA-dPMMA layer on the nickel.
(b) – Excitation spectrum of EuTTA (in solution). It was presented in [15].

In Fig 3.3 the emission spectra for different excitation wavelengths are presented for EuTTA-dPMMA layers coated on nickel (a) and on $La_4Sr_{10}Cu_{24}O_{41}$ (b). For both substrates the emission peak is centered around 612 nm, which agrees well with the previously reported [15] (see also Fig 3.2). For both prepared samples the excitation spectrum is broad with a cut off around 400 nm (Fig 3.4 a), which is in good agreement with earlier measurements [15] (Fig 3.4 b). From this experiment it was found that the most efficient excitation is around 340 nm and the emission detection is around 612 nm.

To measure the absolute temperature change the calibration coefficient α has to be determined. For this purpose we did a measurement of the emission intensity of the EuTTA-dPMMA layer as a function of temperature (Fig 3.5).

The light emission is proportional to the quantum efficiency (QE) which is temperature dependent. The dependence of the quantum efficiency can be analytically expressed as follows [12]:

$$QE(T) = A - Be^{C*T} \tag{3.1}$$

Then the ratio between the light intensity from a hot and a cold sample follows:

$$\ln\left(\frac{I_{HOT}(T)}{I_{COLD}(T)}\right) = \ln\left(\frac{QE_{HOT}(T)}{QE_{COLD}(T)}\right) = \ln\left(\frac{A - Be^{C*THOT}}{A - Be^{C*TCOLD}}\right) \approx C\left(T_{HOT} - T_{COLD}\right) = \alpha\Delta T \tag{3.2}$$

When a surface heats up, the temperature change with respect to the initial temperature T_0 can be calculated from:

$$\Delta T = \alpha^{-1} \ln\left(\frac{I(T)}{I(T_0)}\right) \tag{3.3},$$

where α is the calibration constant (%K^{-1}). From the results of the experiment we determined the calibration constant being α=-0.045±0.002 K^{-1}. This corresponds well with the value α=-0.047 K^{-1} found in the literature [16].

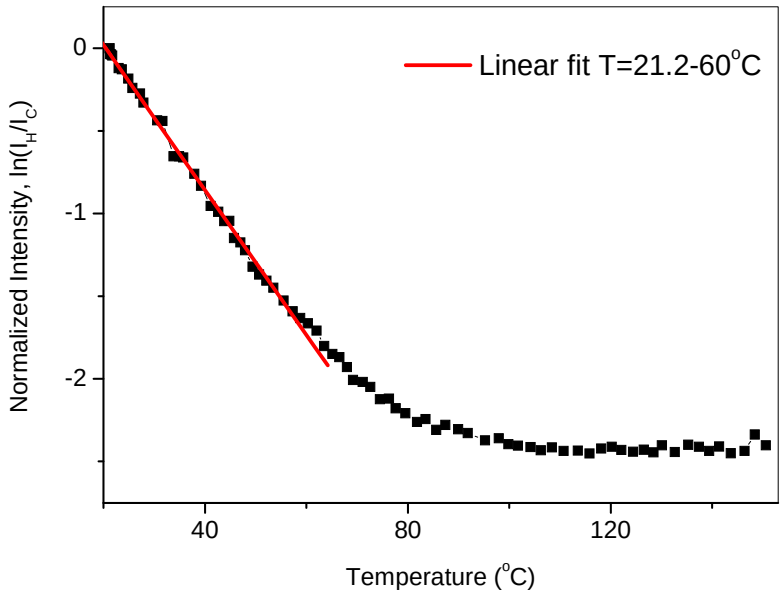

Fig 3.5. The logarithm of the normalized intensity (I_C-intensity at room temperature, I_H-intensity when heated) as a function of temperature.

3.4 Experimental setup

The experimental setup is shown in Fig 3.6. The intensive (~0.4 W) light beam (488 nm) from the Argon-ion laser (Innova 300, Coherent) was used to heat the sample from one side. The heating beam was focused on the sample to 100 μm in diameter. The beam was transmitted through an acousto-optical modulator (AOM, Isomet 1206C-2-1002) to have a possibility to provide pulsed heating. From the other side the sample was radiated with 370 nm light (focused to 50 μm in diameter, 6 mW), which is a result of the second harmonic generation in a LBO non-linear crystal of the 740 nm beam of a pulsed Ti:Sapphire oscillator (80 MHz, 100 fs, 700 mW) (Mira 900, Coherent). The emission from the EuTTA-dPMMA layer was collected into the photomultiplier tube (Hamamatsu R5600P-01). The time of heating and emission detection is synchronized electronically.

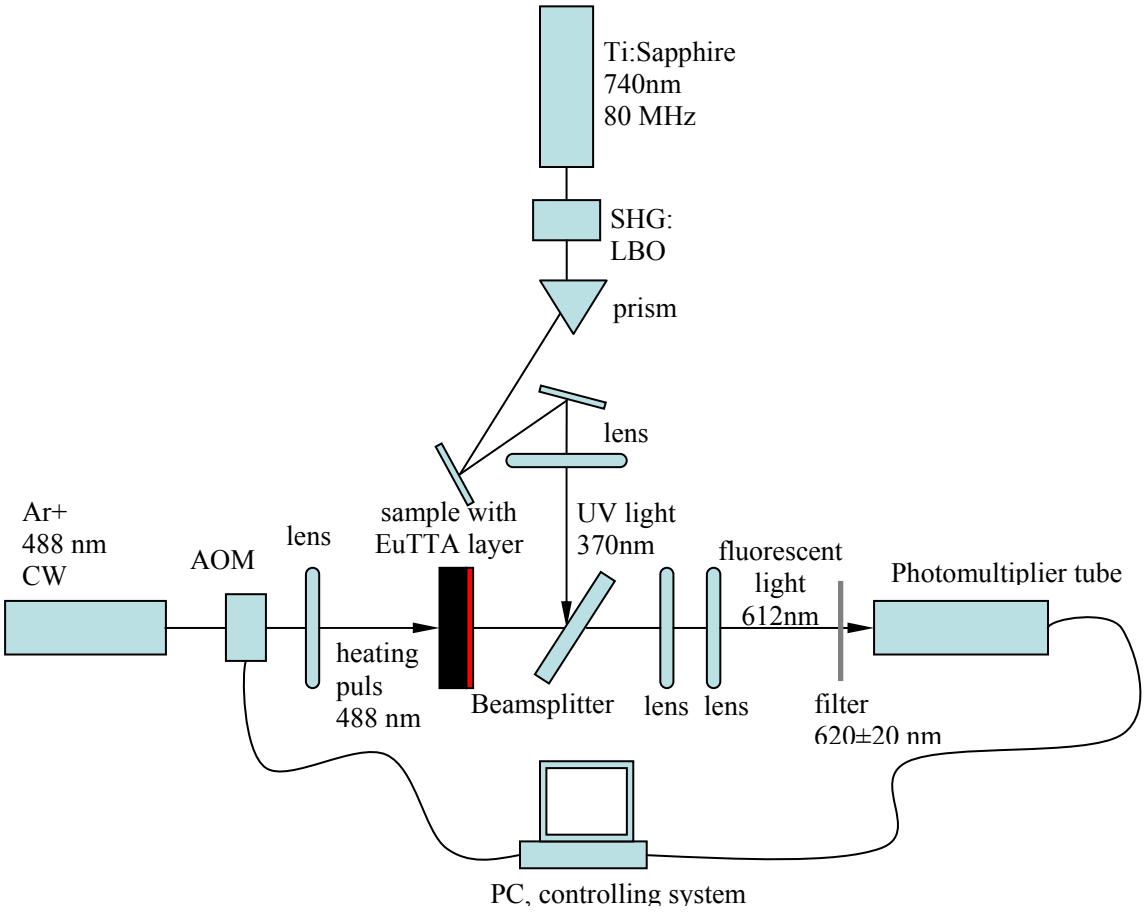

Fig 3.6. The experimental setup

3.5 Characteristics of the experimental setup

The two most important characteristics of our experimental setup were analyzed: the response time and the strength of the output signal.

3.5.1 Response time

The response time is an indication how fast the setup is capable of reacting to the change in signal. The response time for this setup is established by the timing of the switching on/switching off of the AOM and of the response time of the detection system (photomultiplier and consequent electronics). The rise time of the AOM was specified to be around 300 ns [17]. The photomultiplier tube has a specified rise time of around 0,65 ns [18].

In Fig 3.7 the effect of the "leakage" of the heating pulse is shown. The characteristic response time was measured to be around 20 μs, mainly established by the detection electronics used in the experiment (RC time around 10 μs). The point in time the light intensity increased corresponded exactly with the time the heat pulse started. This indicates the timing in the experiment is very well synchronized.

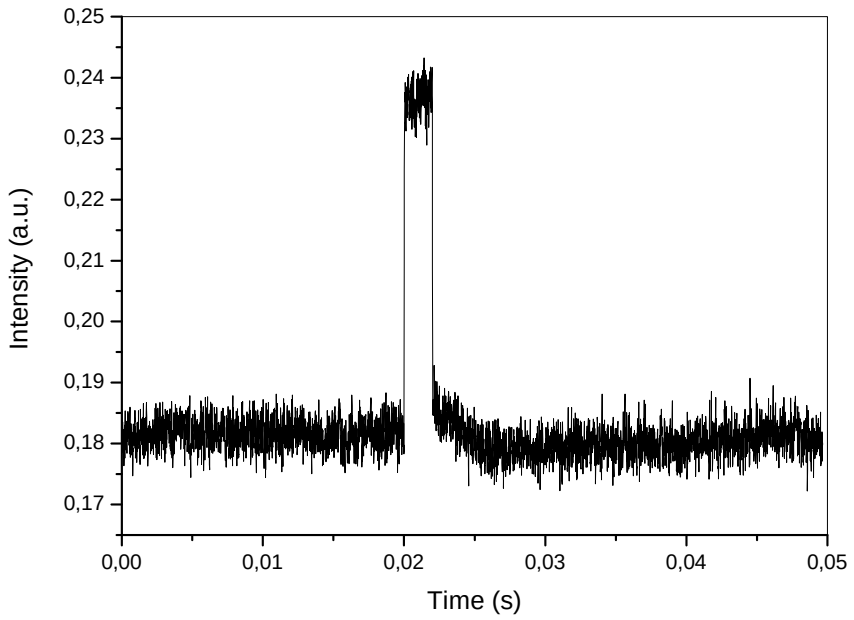

Fig 3.7. The effect of " leakage" of the heating pulse detected by the photomultiplier tube.

3.5.2 Signal strength

It is possible to estimate the signal strength using initial parameters. The power of the 370 nm light at the sample was measured to be P_{UV}=6.0 mW, which corresponds to

$1.1*10^{14}$ photons s^{-1}. Initially it is assumed that the thickness of the EuTTA layer is sufficient to absorb all photons. The fraction of photons re-radiated is given by the quantum efficiency QE(T). It is estimated that QE(20°C)=0.20 [19]. Because changes in the QE are only about 4.5 %/K this value is assumed to be constant.

The 612 nm light is emitted uniformly, but light emitted into the crystal is reflected with reflectivity $R_{crystal}$. All light is collected by a lens with r_{lens}=2.5 cm at a distance d_{lens}=9 cm. When the light travels through a lens, beam splitter or filter it is reflected twice: while entering and exiting. So R_{lens}, $R_{beamsplitter}$ and R_{filter} also have to be taken into account. The light intensity (photons s^{-1}) that is expected to enter the photomultiplier tube is:

$$I_{PT} = I_{UV} \times QE(T) \times (1 + R_{crystal}) \times \frac{\pi \times r_{lens}^{2}}{4\pi \times d_{lens}^{2}} (1 - R_{beamsplitter})^2 (1 - R_{lens1})^2 (1 - R_{lens2})^2 (1 - R_{filter})^2 \quad (3.4)$$

The reflectivity of the crystal is estimated to be $R_{crystal}$=0.20 [20]. The other elements are made of glass which generally has a reflectivity $R_{beamsplitter}$= R_{lens}= R_{filter}=0.04. From these estimations, it follows I_{PT}=$3.7*10^{13}$ s^{-1}, which for λ=612 nm corresponds to a power P_{PT}=12 μW.

It is specified [18] by the manufacturer that the Hamamatsu 5600U-01, which has the same cathode as the 5600P-01, has a cathode radiant sensitivity of S~23 mA/W. A voltage of 900V was applied, this corresponds to a current amplification of A~$6*10^5$. The current is led through a resistance (R=1 kΩ) over which the voltage is measured. The voltage measured is estimated to be:

$$V = I \times R = P_{PT} \times S \times A \times R \quad (3.5)$$

It follows that the expected voltage to be measured is about V~167 V. However, the signal measured is only about V~0.3-0.4V. This difference can be explained by estimating how many photons falling on the layer are absorbed. The UV-light has a beam radius of r=25 μm. The layer thickness is approximately t=50 nm. The mass density of the EuTTA layer is assumed to be the same as the mass density of dPMMA, ρ=1.19 g/cm^3 [21]. The mass ratio EuTTA:dPMMA = 1:1.36. The mass M of the EuTTA excited is:

$$M = \pi \times r^2 \times t \times \rho \times \frac{1}{1 + 1.36} \quad (3.6)$$

So M=$5.0*10^{-11}$ g EuTTA. The mass of 1 mol EuTTA ρ=869.52 g $mole^{-1}$. So the number of molecules of EuTTA which can be excited is N=$3.4*10^{10}$.

The decay time of EuTTA emission was measured to be t=250 μs. The EuTTA is however excited in pulses of UV light, having an interval of 13 ns and containing $1.4*10^8$ photons. The portion p of the amount of light that is absorbed is therefore:

$$p = \frac{\left(1 - e^{-\frac{13ns}{250\mu s}}\right) \times 3.4 \cdot 10^{10}}{1.4 \cdot 10^{8}} = 1.2*10^{-2}. \quad (3.7)$$

This will result in a expected signal of V~2.1 V, which is only a factor 5 different from the measured value.

4 Results and Discussions

4.1 Experiments

The final experiments were performed on a nickel sample, $Ca_9La_5Cu_{24}O_{41}$ (denoted as Ca_9La_5) and $La_4Sr_{10}Cu_{24}O_{41}$ (denoted as La_4Sr_{10}). The parameters of the performed experiments are shown in Table 4.1. Due to losses at optical elements, the power P_{eff} that fell onto the sample was lower than the output power P_{laser} of the Argon-ion laser, so the effective power was measured separately.

There is a certain delay time t_d before heat was applied in each measurement. The sample was heated during a certain time t_{heat} and the total measurement time was t_{exp}. To let the sample cool down again there was an interval time t_i between subsequent measurements. A total number of N measurements were performed per sample. For the first measurement performed with Ca_9La_5 some 488 nm light from the heat pulse "leaked" into the photomultiplier tube. The data was corrected for this "leakage".

n	Sample type	radius (mm)	thickness (mm)	P_{laser} (W)	P_{eff} (mW)	t_d (ms)	t_{heat} (ms)	t_{exp} (ms)	t_i (s)	N	Remarks
1	Ca_9La_5	1	0.39	4.0	350	20	10	500	5	100	leakage
2	Ca_9La_5	1	0.39	4.0	350	20	10	200	5	101	-
3	La_4Sr_{10}	2.25	2.63	4.0	350	40	100	1000	5	99	-
4	Nickel	4.5	1.60	5.0	438	100	600	1000	5	85	-

Table 4.1. Measurement parameters

It was found that the average light intensity during the delay time decreased after each measurement. This is due to bleaching of the EuTTA-layer, the quantum efficiency decreases when the layer is exited for a longer period of time. The precise mechanism is however not fully understood. To correct for this effect each measurement was normalized to the average light intensity during the delay time.

For each series of measurements the average of all N measurements was calculated. This way the noise level is reduced by a factor $\sqrt{N}$. The relative temperature change is calculated using equation (3.3). The previously found calibration constant α=-0.045 K^{-1} is used (section 4.3). It is assumed that bleaching does not affect the calibration constant. The noise present in the resulting graph is most likely due to shot and thermal noise in the electronic signal. This is probably caused by the relatively low signal strength. By applying a Fourier low frequency filter the average curve, that roughly goes through the middle of the noise, can be determined, so its features can be seen more clearly.

4.2 Sample heating

As an example the obtained graph for the temperature $La_4Sr_{10}Cu_{24}O_{41}$ is shown (Fig 4.1). From t=0 s until t=0.10 s the heat pulse is applied. It can be seen that it takes a certain amount of time before the temperature starts rising, the maximum temperature rise is reached some time after the heating has stopped and afterwards the sample starts cooling down.

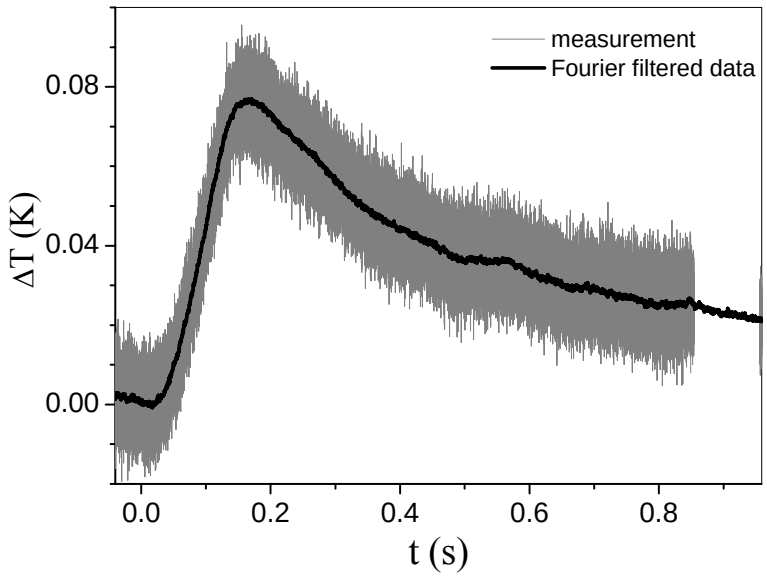

Fig 4.1. The measured rise in temperature and the cooling down at the back of the $La_4Sr_{10}Cu_{24}O_{41}$ sample as a function of time. A heat pulse is applied from t=0 s until t=0.10 s.

In the graphs of the temperature change it can be seen that after heating each sample, the temperature does not seem to decay back to zero, but to some positive value. The heat that is applied to the sample needs some time to diffuse throughout the sample and results in a rise in average temperature. The expected rise in temperature can be estimated from:

$$\Delta T_{calc} = \frac{(1-R)*E}{C_V * V} \qquad (4.1)$$

Here E is the amount of energy added, C_V is the specific heat and V is the volume of each sample. R is the reflectivity.

The specific heat C_V=1677 J $mol^{-1}K^{-1}$ was measured for Ca_9La_5 in the group of C. Hess in Dresden [23]. Note: this was measured in mole unity cells. It is assumed that this value is the same for La_4Sr_{10} and assuming the size of a unit cell is also the same for both crystals, 4.18 $Å^3$ [7], the specific heat C_V (J cm^{-3} K^{-1}) is calculated. The specific heat for nickel is C_v=3.9566 J cm^{-3} K^{-1} [6].

The reflectivity for $Sr_{14}Cu_{24}O_{41}$ is measured to be approximately 0.2 [20]. It is assumed that $Ca_9La_5Cu_{24}O_{41}$ and $La_4Sr_{10}Cu_{24}O_{41}$ have the same value, because the crystal structures are similar. In the case of the nickel sample the surface was colored with a black marker to improve the absorption. So the reflectivity is assumed in the calculation to be 0. By fitting an exponential decay to the graphs of the temperature, it can be found to which temperature ΔT_{exp} the temperature of the sample is stabilizing after heating. The maximum measured rise in temperature is denoted as ΔT_{max}. The results are shown in Table 4.2.

Sample	C_V (J cm^{-3} K^{-1})	V (cm^3)	R	E (J)	ΔT_{calc} (K)	ΔT_{exp} (K)	ΔT_{max} (K)
Ca_9La_5 (1)	0.665	0.00039	0.2	0.0035	10.8	0.292	1.52
Ca_9La_5 (2)	0.665	0.00039	0.2	0.0035	10.8	0.169	0.80
La_4Sr_{10}	0.665	0.0418	0.2	0.035	1.27	0.0174	0.074
Nickel	3.9566	0.102	0	0.263	0.653	0.233	0.37

Table 4.2. Rise in temperature as calculated and measured.

As can be seen, the rise in temperature of the crystal is less than what can be expected when all the applied heat is absorbed and spreads uniformly throughout the sample. Also the maximum heating is less than this minimum expected value.

An explanation is that less heat is actually applied to the sample, because the reflectivity at the surface is higher than initially assumed. In the case of the nickel sample the surface was colored with a black marker to improve the absorbance. As the results for nickel correspond better, this possibly had a great effect on the amount of heat absorbed compared to the other samples. Another explanation is that heat escapes the crystal after it is heated. This can be due to radiation or heat conduction via the sample holder. The rate is however dependent on the temperature difference with the environment and only at the surface where the sample is heated this temperature difference can be big enough to explain the discrepancy for Ca_9La_5 and La_4Sr_{10}. Possibly a lot of energy radiates out of the sample at the place it is heated.

4.3 Simulation

When translating the differential equations (2.4, 2.5) into a simulation, the Peaceman-Rachford scheme is used for the 2-dimensional case, with the cylindrical coordinates. The simulations are done using cylindrical coordinates because there are only three coordinates (r, z, t) instead of four (x, y, z, t), so this simulation goes faster. It is found the final results are not significantly different. How this Peaceman-Rachford scheme works exactly will not be discussed in detail. For details see [24]. This method combines a second-order accuracy in time with stability when larger time steps are used.

In the simulation the dimensions of the crystal are specified by (r, Δr, z, Δz). r is the radius of the crystal and z is the thickness. Δr and Δz are the step sizes the crystal is divided into. The diffusion constants (D_r, D_z) are specified for the radial and the z-direction. Starting at t=0 s, heat is added for a certain duration with a specified power (a.u.). Heat is added according to $\exp(-z/ z_o)$, with z_0 the penetration depth. The program simulates the temperature at the side of the crystal opposite to the heated side and at the center of the crystal. The temperature is simulated during a time t in steps of Δt. The change in temperature is dimensionless, because the specific heat is not known exactly for all crystals and the exact amount of heat added is also unknown. The output therefore has to be rescaled with a factor to fit the experimental results.

For the simulation it is necessary to know how deep the light penetrates the sample. The penetration depth δ, or skin depth, is defined as the depth at which the intensity has decreased to 1/e of its initial value [25] and it follows that:

$$\delta = \frac{2}{\alpha} = \frac{2c}{2\omega\sqrt{\varepsilon_2/2}} \tag{4.2}$$

Here α is the attenuation constant and ε_2 is the imaginary part of the dielectric coefficient. It was reported [20] for $Sr_{14}Cu_{24}O_{41}$ that for light with a wavelength of λ=488 nm, ε_2=3.33. This gives $\delta=6.02*10^{-2}$ μm. Because $Ca_9La_5Cu_{24}O_{41}$ and $La_4Sr_{10}Cu_{24}O_{41}$ structurally do not differ a lot, it is assumed that these two compounds have the same penetration depth. For Nickel the penetration depth is found to be δ=14 nm (for 740-805 nm light) [26] and it is assumed it will not differ a lot for λ=488 nm. These values are necessary for the simulation, although their effect on the final outcome is not very big, because δ is very small compared to the step size Δz=0.010 mm the crystal is divided into.

The dimensions of the samples were measured. The thickness of Ca_9La_5 was not uniform. In the center the thickness was 0.40 mm but near the edges 0.36 mm. Because the measurements were performed near the center a thickness of 0.39 mm is assumed. The surfaces were assumed to be circular by approximation. The radius of the heating laser was estimated to be 50 μm. The used parameters for the samples are summarized in Table 4.3. R and Z were taken with step sizes of Δz=Δr=0.01 mm. The temperature was calculated in step sizes Δt=50 μs.

Crystal	Radius R (mm)	Thickness Z (mm)	Penetration depth (nm)	Heating radius (μm)	Heating time (ms)
Ca_9La_5	1	0.39	60	50	10
La_4Sr_{10}	2.25	2.63	60	50	100
Nickel	4.5	1.60	14	50	600

Table 4.3. Crystal parameters

Comparing the measured results with the results of the simulation program, diffusion constants were determined from the best fits. While doing the simulations it was found that the beginning of the simulation curve, especially the moment the temperature starts rising and the moment the maximum temperature is reached, is mainly determined by the value of D_z. D_r influences the moment the maximum temperature is reached to a certain extent, but mostly determines the rate with which the temperature decreases after the heat pulse. The heat losses, neglected in the simulation, start to play a role in the measurement after some time, so D_z could in general be determined more accurately than D_r.

4.3.1 Nickel

When it was tried to find a simulated curve that fits the results for nickel, it was found impossible to fit the measured data over the entire domain.

First the simulation curves were tried to fit as good as possible with the data only for the first 0.10 s (Fig. 4.1). 0.10 s was approximately the longest time for which a good fit was possible. The best fit has $D=D_r=D_z=18\pm3$ mm^2s^{-1}. D_r and D_z have to be the same because nickel is isotropic.

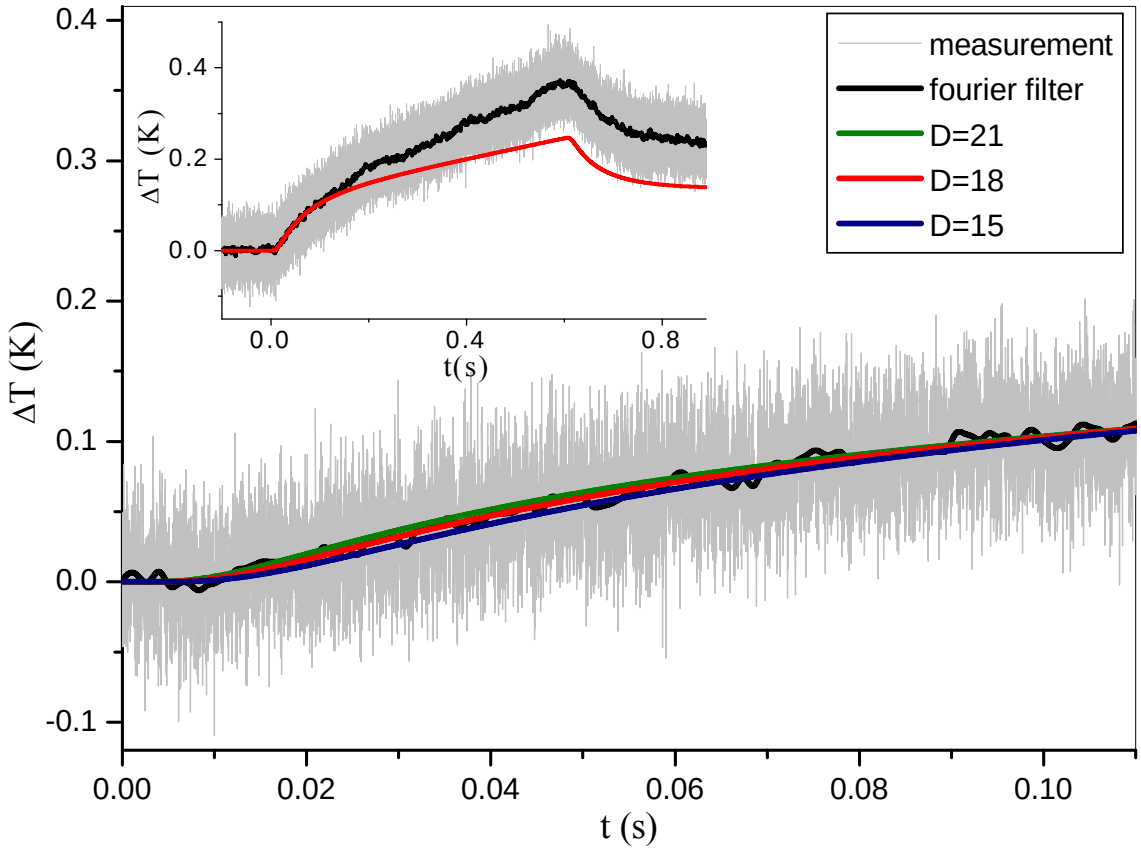

Fig 4.1. Fit over the first 0.10s for the measurement with nickel as function of $D=D_r=D_z$ (in mm^2s^{-1}). Inset: The full measurement, showing a rise in temperature during the heat pulse and cooling down after the heat pulse stopped.

The final rise in temperature according to the simulation is lower than measured. It is however expected to be equal or higher, because no heat losses are taken into account in the simulation. For the second fit the simulation curves therefore were assumed to have a final rise in temperature equal to the measured maximum rise in temperature (Fig. 4.2).

Now the best fit has $D=D_r=D_z=16\pm4$ mm^2s^{-1}. When the temperature rise in the simulation is assumed to be higher than the measured maximum rise in temperature, the value for the diffusion constant becomes even lower.

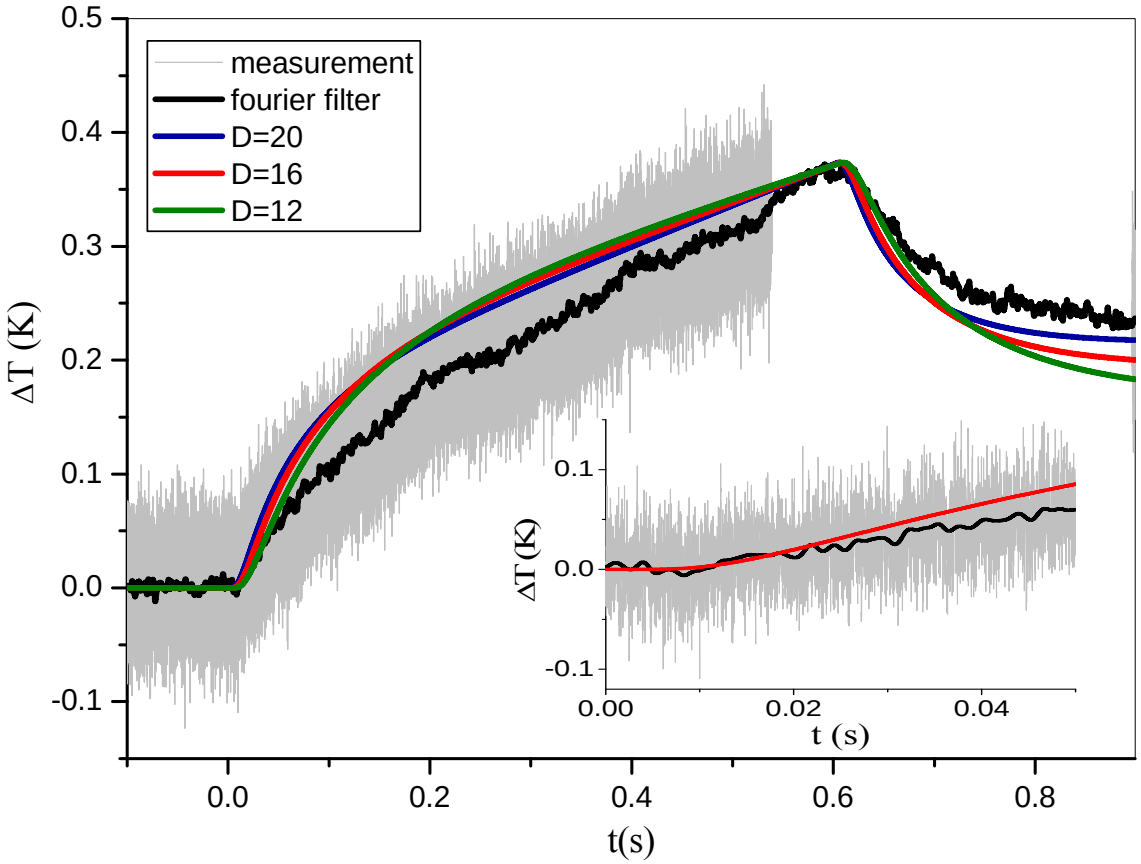

Fig 4.2. Fit for the measurement with nickel as a function of $D=D_r=D_z$ (in mm^2s^{-1}), when the simulation curve has the same maximum rise in temperature as measured. Inset: Part of the curve where the temperature starts rising.

4.3.2 First measurement $Ca_9La_5Cu_{24}O_{41}$

Because it was not possible to obtain a fit in the entire measurement region, it was tried to make the simulation curve fit the data over an as long as possible time domain. The simulation curves fit with the data for approximately the first t~0.3 s (Fig. 4.3). The best fit has D_z=8.3±1.8 mm^2s^{-1} and D_r=0.014±0.006 mm^2s^{-1}.

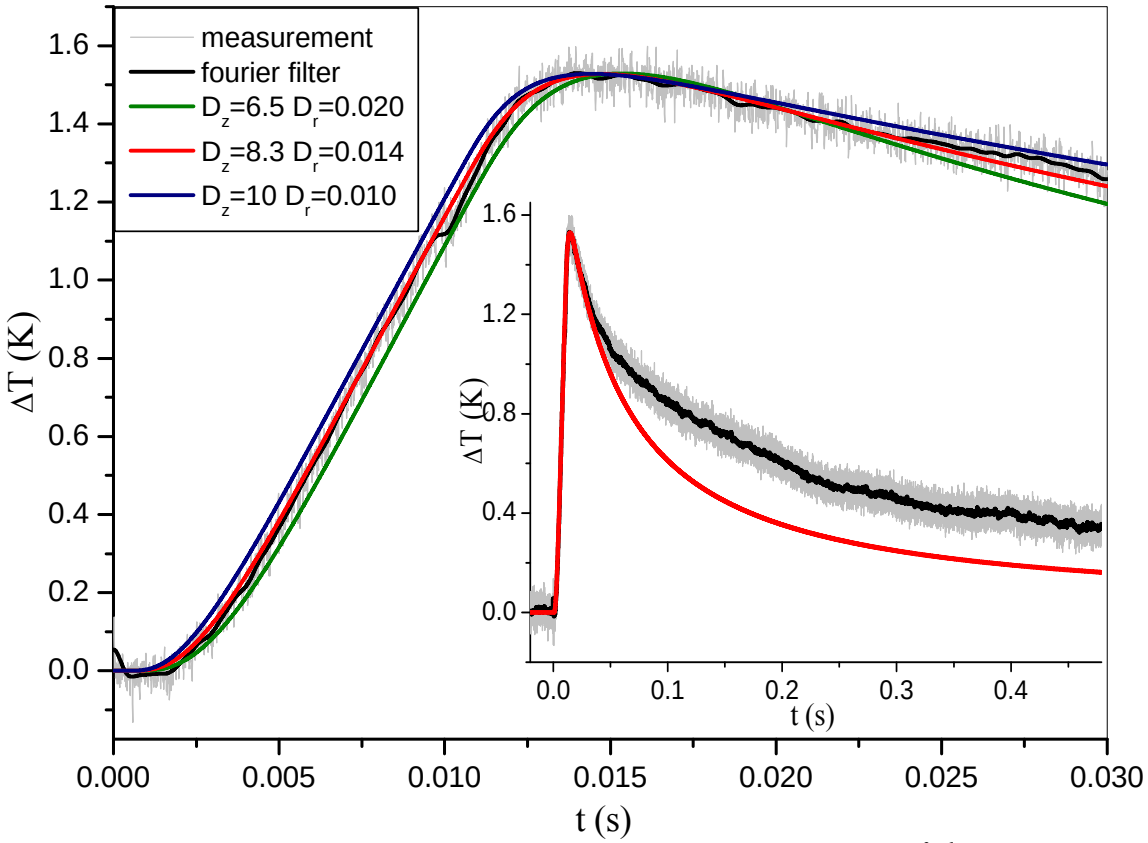

Fig 4.3. Fit for the first measurement with $Ca_9La_5Cu_{24}O_{41}$ as function of D_z and D_r (in mm^2s^{-1}). Inset: The heating up and cooling down during the entire measurement plus the best fit.

4.3.3 Second measurement $Ca_9La_5Cu_{24}O_{41}$

It was found possible to fit simulation curves with the data over the entire measurement domain (Fig. 4.4). The best fit has D_z=9±3 mm^2s^{-1} and D_r=0.006±0.003 mm^2s^{-1}.

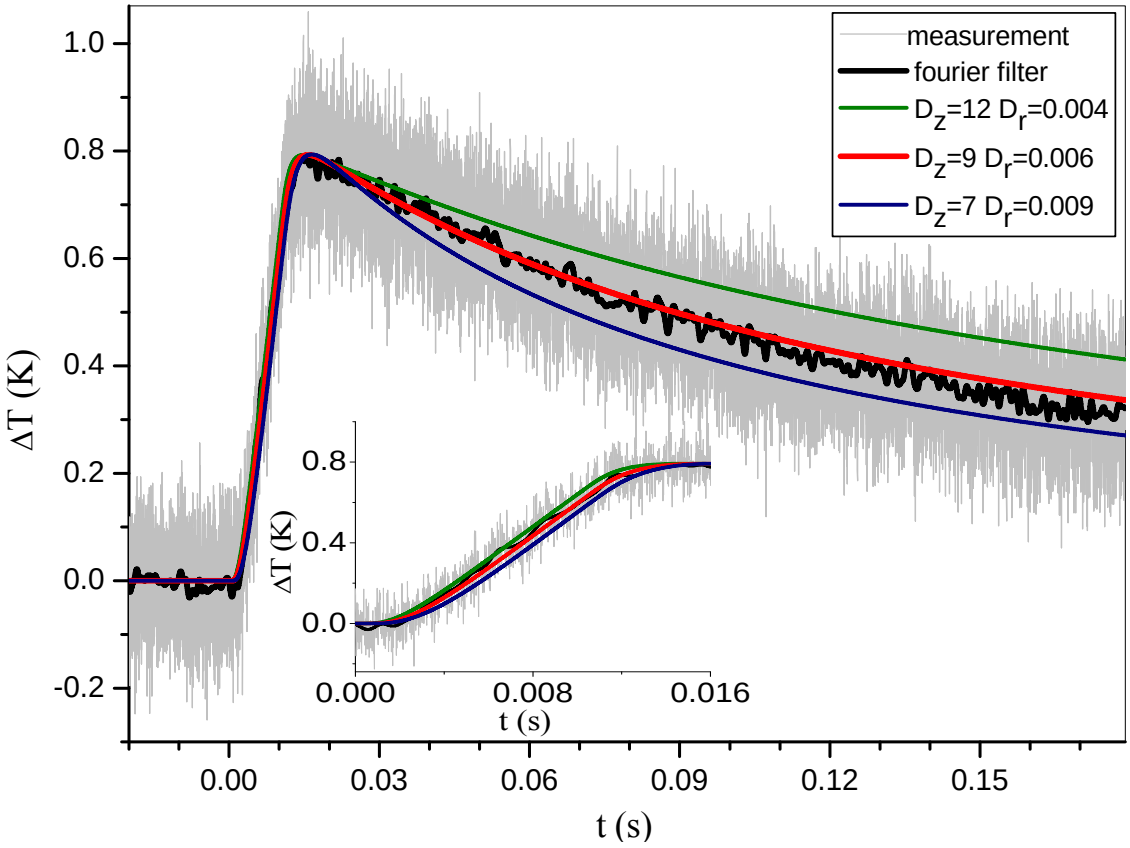

Fig 4.4. Fit for the second measurement with $Ca_9La_5Cu_{24}O_{41}$ as function of D_z and D_r (in mm^2s^{-1}).

4.3.4 $La_4Sr_{10}Cu_{24}O_{41}$

Because it was not possible to obtain a fit over the entire measurement, it was tried to make the simulation curve fit the data over an as long as possible time domain. The simulation curves fit with the data until approximately t~0.25 s (Fig. 4.5). The best fit has D_z=12.3±1.8mm^{2}s^{-1} and D_r=6±1mm^{2}s^{-1}.

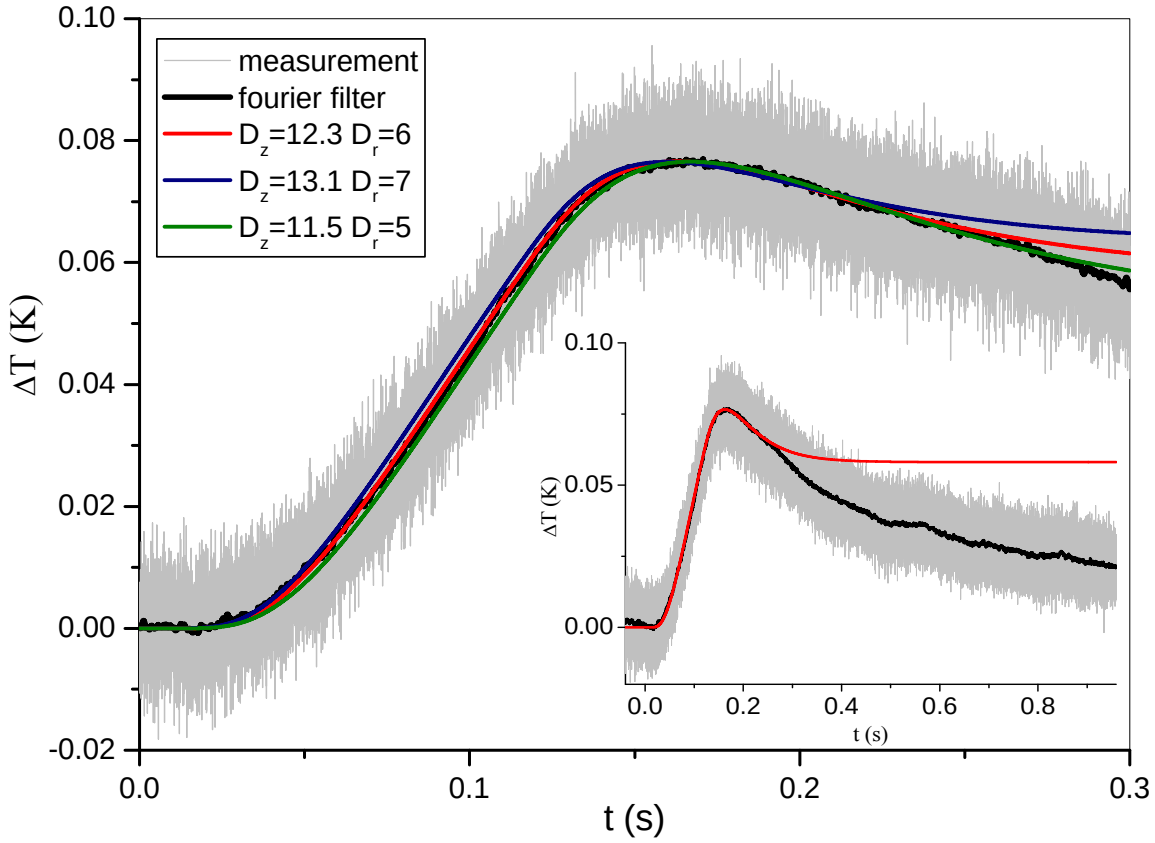

Fig 4.5. Fit for the measurement with $La_4Sr_{10}Cu_{24}O_{41}$ as function of D_z and D_r (in mm^{2}s^{-1}). Inset: Rise in temperature during the entire measurement.

4.4 Discussion

In formula (4.3) it is given that the heat diffusion constant D_i is equal to:

$$D_i = \frac{\kappa_i}{\rho C_p} \tag{4.3}$$

In the literature it is found that for pure nickel the thermal conductivity κ=90.9 $Wm^{-1}K^{-1}$, the density ρ=8.908 gcm^{-3}= 1.5177 $molcm^{-3}$ and $C_P \approx C_V$=26.07 $Jmol^{-1}K^{-1}$ [6]. Using formula (4.3) it is calculated: D=23 mm^2s^{-1}.

The thermal conductivity was measured for $Ca_9La_5Cu_{24}O_{41}$ to be κ_c=93 $WK^{-1}m^{-1}$, κ_a=3 $WK^{-1}m^{-1}$ [4] C_p=1731 JK^{-1}mol (unit cells)$^{-1}$ [23] and the volume of a unit cell is 4253 $Å^3$ [27]. Using formula (4.3), it is calculated: D_c=138 mm^2s^{-1} and D_a=4.4 mm^2s^{-1}. (Note: the c-direction is along the spin ladders, z-direction in the simulation. The a-direction is perpendicular to the spin ladders, r-direction in the simulation.).

For $La_4Sr_{10}Cu_{24}O_{41}$ the thermal conductivity has not been measured. The thermal conductivity perpendicular to the spin ladders is expected to be about the same as for $Ca_9La_5Cu_{24}O_{41}$, because it is also due to heat transport by phonons and the crystal structure is quite similar. D_c is unknown, but is expected to be larger than D_a.

The final results for the diffusion coefficients obtained in this work and from literature data are summarized in Table 4.4.

Measurement	D_c (mm^2s^{-1}) Literature data	D_c (mm^2s^{-1}) This work	D_a (mm^2s^{-1}) Literature data	D_a (mm^2s^{-1}) This work
Nickel, fit initial part	23	18±3	23	18±3
Nickel, fit height	23	16±4	23	16±4
$Ca_9La_5Cu_{24}O_{41}$ 1st measurement	138	8.3±1.8	4.4	0.014±0.006
$Ca_9La_5Cu_{24}O_{41}$ 2nd measurement	138	9±3	4.4	0.006±0.003
$La_4Sr_{10}Cu_{24}O_{41}$	Unknown	13.1±1.8	4.4 (estimated)	7±1

Table 4.4. Summary of the values for the diffusion coefficient D, obtained from the calculations and fitting simulation curves to the measurements.

In general the literature results and the values for the diffusion constant found in this work differ from each other.

The measurements with nickel were performed as test measurements, because the value for the diffusion constant D is known accurately, but the value found using our method differs ~20% from the literature value [6]. The literature value is however for pure nickel. Although the used sample is expected to have a high purity too, possible defects in the crystal structure cannot be ruled out. Because the heat transport occurs mainly by free electrons, defects will decrease the heat transport. This possibly explains the difference.

The simulation fits the measurements very well for the first t~0.10 s, but predicts the final rise in temperature to be only ~70% of the measured final rise in temperature. When the simulation does correspond to the final rise in temperature, the simulation curve does

not fit the measurement well, especially during the heating of the sample, and the value for D is lower than expected.

The nickel is heated via a (very thin) black, absorbing layer, which influences the speed with which heat is applied. But this influence is expected to be very small. Also it cannot be ruled out that the crystal has not cooled down entirely prior to each measurement, especially in the center. The influence of this on the subsequent measurement is unknown. Possibly there are other unknown imperfections in the used experimental method.

More measurements need to be done to clarify the mechanism(s) responsible for the discrepancy between measurement, simulation and literature.

The simulations of the two measurements with $Ca_9La_5Cu_{24}O_{41}$ find a consistent value for D_c, but not for D_a. The used sample is relatively small and irregularly, triangularly shaped. In the simulation it was however assumed to be disk shaped. The shape of the boundary is of influence of the heat diffusion in the r-direction, so it is expected the values found for D_a are different from what is expected [4, 23, 27]. But why the values are only 0.3/0.1% of the expected value is unknown. Possibly one of the causes is that defects in the lattice have distorted the phonons.

D_c is mainly determined by fitting the beginning of the simulation curves to the measurement. These fits are expected to be more accurate, because in the beginning of the heating the boundaries play a less important role, as the heat has not yet diffused a lot in the r-direction. The value for D_c is however only ~6% of the expected value. Because the value for D_c is about twice the expected value for D_a, it is possible the magnons only contribute for 50% or less to the heat transport. The crystal could be less pure than the crystal of which the thermal conductivity was measured in a traditional way [4]. Also the crystal could have been misaligned, so the spin ladders were possibly not aligned in the z-direction.

The measurements by traditional means were performed using the direct heat transport method, where the temperature drop over a sample is measured for a constant heat current [4]. Possibly the fact the sample is heated in pulses of 10 ms cause the magnons to be less effective heat transporters, because the magnons need some time to be created, although this time is expected to be smaller than the time scale of the experiment.

Still it can be concluded that anisotropic heat transport occurs, because the value found for D_c is larger than D_a (although it is not certain if this value is correct) and, most important, the value found for D_c is approximately twice as large than the expected value for D_a, which is only due to phononic heat transport. So it can be concluded there is anisotropic heat transport, most likely due to magnons. The reason for the discrepancy in the value for D_a is not exactly known.

The results for $La_4Sr_{10}Cu_{24}O_{41}$ seem to be good, because the simulation curves fit the measurement well for both the heating up of the crystal and some amount of time during which the heat spreads throughout the crystal. As expected the simulation starts to fail once the heat has spread throughout the entire crystal and the cooling down at the boundaries becomes of greater influence.

The value for D_r is ~60% higher than the expected value [4, 23, 27] but this was for a different crystal. So it can be that heat transport due to phonons is more effective for this

crystal. The value for D_c is twice as high as D_a, so there is indeed anisotropic heat transport. The value is however not as high as was measured for $Ca_9La_5Cu_{24}O_{41}$, [4,23,27]. It can be that heat transport by magnons is less effective in this crystal, although there is no reason to expect it to be ~90% smaller than the value previously reported, because the crystals are quite similar. As mentioned earlier, the value for D_c can also be too low due to imperfections, misalignment or the possibility magnons being less effective heat transporters when the heat is applied in pulses.

Again it can be concluded that there is anisotropic heat transport, most likely due to magnons.

4.5 Suggestions for future improvements

There are several suggestions to possibly improve the accuracy of the measurements.

First, it can be tried to improve the strength of the signal, because the relative amount of noise will decrease when increasing the signal strength. This can be done by making the EuTTA layer thicker, but then there is a risk the response to the change in temperature of the outer layer of the sample will decrease. So the ratio between the thickness of the EuTTA layer and the sample thickness has to remain sufficiently small. The ratio EuTTA:dPMMA can be increased further, but still a stable matrix has to be formed. The intensity of the UV light can be increased, but because not all photons were absorbed in the first place (see section 3.5.2) this may not make a very big difference. Exciting the layer with a different wavelength may increase the light output with roughly 10%, so this is not of great influence either (see section 3.3). It can be tried to collect more light, for example by using only one lens with a larger NA or removing the beam splitter. It can be examined if it is really necessary to shine the UV light perpendicular to the sample surface, otherwise the UV light can be shone on the sample under an angle so the beam splitter can be removed. When taking the average over even more measurements the noise can be reduced further, but at the cost of a longer measurement time.

Second, it can be tried to make the simulations of the measurements more realistic. It can be tried to take into account heat losses, for example by using theory of black body radiation. By taking samples with a very large ratio of r/z (r being the radius and z the thickness of the sample), the samples will approximate an infinitely big disk better and the relative effect of heat losses at the edges will decrease. It was not certain if the samples were entirely cooled down after each measurement, so it can be tried to cool the samples down longer.

The simulation program can be modified to calculate the absolute rise in temperature throughout the sample. For this it will be necessary to accurately know the specific heat, which can be measured, but especially how much heat is applied. As was shown in Table 4.2, the absorbed amount of heat was smaller than expected. A thin, all heat absorbing layer applied on each sample might help to solve this problem. Also it will be necessary to determine accurately over which area the temperature is measured. When the ratio r_{heat}: r_{UV} is increased (with r_{heat} being the radius of the heat pulse and r_{UV} the radius of the

ultraviolet light beam), the simulation will also be more accurate in determining D_z, because the influence of heat diffusing in the r-direction will become less.

It can be tried to completely eliminate the effect of heat diffusion in the r-direction by equally heating the entire surface of a sample. The rise in temperature on the other side will be the same over the entire surface, so UV-light can now be shone on the complete area, thereby improving the signal strength. The theoretical fitting curves can now be obtained using Parker's formula, which describes the normalized temperature response for one dimensional heat diffusion [28], so no simulation will be needed any longer to determine D_z. It will be necessary to have enough laser power to heat up the sample in a detectable way. Difficulties may also arise to heat up the surface uniformly, as the laser produces a Gaussian shaped beam which will have to be deformed.

5 Conclusion

An experimental setup was build with which the heat diffusion through several samples could be measured. By taking the average over a large (80-101) amount of measurements, the rise in temperature at the side opposite to the heated side, was measured using the fluorescent microthermal imaging technique. By fitting simulation curves to the measurement the heat diffusion constants were determined, see Table 4.4.

The measured D for the nickel sample is slightly lower than the previously reported value [6]. This can be due to possible impurities in the used sample.

For the $Ca_9La_5Cu_{24}O_{41}$ sample a large anisotropic heat conduction was shown, most likely due to heat transport by magnons along spin ladders. The measured values are smaller than earlier reported [4, 23, 27]. This is possibly due to the relatively small size and irregular shape of the crystal, surface effects or imperfections in the crystal.

The crystal of $La_4Sr_{10}Cu_{24}O_{41}$ also shows an anisotropy in the heat conduction originating most likely from heat transport by magnons along spin ladders. The found values of D seem to be physically reasonable, but there are no earlier measurements to refer to.

The measurement technique could be improved by trying to equally heat the sample over the entire surface. Also the signal strength can be improved in various ways, reducing noise.

Acknowledgments

I would like to thank the following people without whom my bachelor thesis would not have been possible. Marian Otter for her guidance throughout the entire work, Ben Hesp with his help with the experiments, Foppe de Haan for his technical support and writing the simulation program, Victor V. Krasnikov and Dmitry Fishman for their help with the experiments and writing the report and Prof. dr. ir. Paul H. M. van Loosdrecht for his guidance.

Bibliography

[1] R.S. Eccleston, Phys. Rev. Lett. Vol 73, 19 (1994)
[2] F. Bloch, Z. Physik 61 ,206 (1930)
[3] E. Dagotto, Rev. Mod. Phys. 66, 763 (1994)
[4] C. Hess. Phys. Rev. B, vol 64, 184305 (2001)
[5] http://www.novmag.eu
[6] http://en.wikipedia.org/wiki/Nickel
[7] Haiying Chen, Physica C 337 p317-321 (2000)
[8] C. Hess, J. of Magn. and Magn. Mat. 290-291 322-325 (2005)
[9] C. Hess, EPJ, vol 15, nr 1 dec 2007, p73-83
[10] P. Kolodner, J.A. Tyson, Appl. Phys. Lett. 40, 782 (1982)
[11] P, Kolodner, J.A. Tyson Appl. Phys. Lett. 42, 117 (1983)
[12] D.L. Barton, P. Tangyunyong, Microelectronic Engineerin 31 p271-279 (1996)
[13] http://www.fkf.mpg.de/crystal/d1-tsfz.pdf
[14] U. Ammerahl, J. Cryst. Growth, 193 (1998) 55; U. Ammerahl and A. Revcolevschi, J. Cryst. Growth, 197 (1999) 825.
[15] H. Winston, J. Chem. Phys., vol 39, no. 2, pp. 267-270 (july 1963)
[16] S.W. Allison, G.T. Gillies, Rev. Sci. Instrum., 68 2615 (1997)
[17] http://www.isomet.co.uk/FinalWebSite/PDFDocs/AO%20Sheets/1206C-2-1002.pdf
[18] http://www.datasheetarchive.com/preview/2873102.html
[19] M. Bhaumik, J. Chem. Phys., vol 40, 3711 (1964)
[20] Z.V. Popovic, Cond. Matt., 0005096v1, (4 may 2000)
[21] http://en.wikipedia.org/wiki/Acrylic_glass
[22] M. Matsuda et al, JAP vol 87 9
[23] private communication, N. Hlubek, IFW Dresden
[24] Numerical Partial Differential Equations-Finite Difference Methods, J.W. Thomas, Springer
[25] http://en.wikipedia.org/wiki/Penetration_depth
[26] Thin Film Non-Noble Transition Metal Thermophysical Properties, AP Caffrey, PE Hopkins, JM Klopf, PM Norris, Microscale Thermophysical Engineering, 8: 365-377
[27] Journal of crystal growth 993 (1998) p55-60
[28] W. J. Parker, R. J. Jenkins, C.P. Butler, and G. L. Abbot, J. Appl. Phys. 32:1679 (1961)
[29] N. Araki, D. W. Tang, and H. Kawashima, Int. J. Thermophysics, Vol. 23, No. 1, p245-252, (Jan 2002)
[30] T. Vuletic *et al.*, Physics Reports 428, p169 – 258, (2006)


Microsoft
PowerPoint Prese